netic frustration. For example, recent theoretical work on the single-band Hubbard model on the triangular lattice suggests that a gapless spin liquid phase is realized at intermediate correlations (8). It is also predicted that the spin liquid phase has both spin-zero and non-zero low energy excitations (21) and incommensurate short-range correlation (22), which may be related to these observations.

Another possibility is a delicate form of long-range order that is dynamically inaccessible in real materials because of impurity pinning close to quantum criticality. Other possible ground states include a Kosterlitz-Thouless (KT) phase driven by two-valued vortices with the transition around T_{peak} (23) and a long-range order without long-range spin correlations such as in a spin nematic (24). The KT phase discussed here is not a conventional one but has a finite spin-correlation length, consistent with our observations. The neutron scattering data show that a large part of the magnetic spectral weight is associated with a long time scale that exceeds 0.3 ns. Experiments characterizing slow spin dynamics are in progress to distinguish between these exotic potential ground states in $NiGa_2S_4$.

Like the spin-1/2 chain in one dimension (1), the triangular lattice antiferromagnet, which is the only geometrically frustrated 2D Bravais lattice, plays a central role in the search for cooperative phenomena in two dimensions. With AF nearest-neighbor interactions, Ising spins have residual entropy (25), and classical Heisenberg spins have a KT-type transition and noncolinear Néel order at $T = 0$ (23). In the extreme quantum spin-1/2 case, a superposition of singlet coverings constituting a resonating valence bond state was first introduced to describe the ground state of the triangular lattice antiferromagnet (3). Although it is now believed that a nearest-neighbor Heisenberg spin-1/2 model has 120° order at $T = 0$ (4–6), one may expect various exotic phases in real materials, driven by other effects such as longer range interactions, multiple-spin exchange, and structural dimerization. Consequentially, there have been intensive experimental searches for an ideal quasi-2D triangular lattice antiferromagnet with a small spin quantum number ($S \leq 1$) (26). Several spin-1/2 triangular lattices have been reported to show nonordered gapless phases, but all the materials so far have either a distorted structure (9, 27) or are only available in minute quantities, which limits accessibility for many experimental techniques (12).

To our knowledge, $NiGa_2S_4$ is the first low spin ($S \leq 1$), quasi-2D bulk magnet on an exact regular triangular lattice. Our measurements on $NiGa_2S_4$ demonstrate that geometrical frustration can be used to stabilize a spin-disordered state at low temperatures. A strongly fluctuating spin state has been discovered in a triangular lattice plane that is isostructural to the superconducting CoO_2 layer of $Na_xCoO_2 \cdot yH_2O$

(14) and isostoichiometric with NiS_2, a metal-insulator transition system (28). It may thus be possible to drive $NiGa_2S_4$ into a conducting state in which the magnetic fluctuations have a qualitative effect on carrier correlations.

References and Notes
1. I. Affleck, *J. Phys. Condens. Matter* **1**, 3047 (1989).
2. A. P. Ramirez, in *Handbook of Magnetic Materials*, K. J. H. Buschow, Ed. (Elsevier Science, Amsterdam, 2001), vol. 13, pp. 423–520.
3. P. W. Anderson, *Mater. Res. Bull.* **8**, 153 (1973).
4. D. A. Huse, V. Elser, *Phys. Rev. Lett.* **60**, 2531 (1988).
5. B. Bernu, C. Lhuillier, L. Pierre, *Phys. Rev. Lett.* **69**, 2590 (1992).
6. L. Capriotti, A. E. Trumper, S. Sorella, *Phys. Rev. Lett.* **82**, 3899 (1999).
7. G. Misguich, C. Lhuillier, in *Frustrated Spin Systems*, H. T. Diep, Ed. (World-Scientific, Singapore, 2004), pp. 229–306.
8. H. Morita, S. Watanabe, M. Imada, *J. Phys. Soc. Jpn.* **71**, 2109 (2002).
9. Y. Shimizu, K. Miyagawa, K. Kanoda, M. Maesato, G. Saito, *Phys. Rev. Lett.* **91**, 107001 (2003).
10. A. P. Ramirez, G. P. Espinosa, A. S. Cooper, *Phys. Rev. Lett.* **64**, 2070 (1990).
11. A. S. Wills, A. Harrison, S. A. M. Mentink, T. E. Mason, Z. Tun, *Europhys. Lett.* **42**, 325 (1998).
12. K. Ishida, M. Morishita, K. Yawata, H. Fukuyama, *Phys. Rev. Lett.* **79**, 3451 (1997).
13. H. D. Lutz, W. Buchmeier, H. Siwert, *Z. Anorg. Allg. Chem.* **533**, 118 (1986).
14. K. Takada et al., *Nature* **422**, 53 (2003).
15. The specific heat, C_p, was measured by a thermal relaxation method down to 0.35 K under fields up to 7 T. In order to estimate the lattice part of the specific heat, C_L, we measured C_p for the isostructural nonmagnetic analog $ZnIn_2S_4$ and obtained the thermal variation of the Debye temperature $\theta_D(T)$ using the Debye equation (29). $\theta_D(T)$ of $NiGa_2S_4$ was then estimated by applying a scale factor according to $\theta_D \propto M_0^{-1/2}V_0^{-1/3}$, where M_0 and V_0 are molar mass and volume, respectively. Finally, C_L was estimated by converting the scaled $\theta_D(T)$ data into specific heat. The magnetic part, C_M, was estimated as the difference between the total specific heat, C_p, and the lattice estimation C_L.
16. P. Sindzingre et al., *Phys. Rev. Lett.* **84**, 2953 (2000).
17. A. P. Ramirez, B. Hessen, M. Winklemann, *Phys. Rev. Lett.* **84**, 2957 (2000).
18. J. Mydosh, *Spin Glasses: An Experimental Introduction* (Taylor and Francis, London, 1993).
19. Neutron diffraction experiments were performed on the Disc Chopper Spectrometer at NIST with 3.55-meV neutrons and an elastic energy resolution of 0.10 meV. Measurements versus T were carried out on the cold neutron triple axis spectrometer SPINS, with an energy of 5 meV and an energy resolution of 0.36 meV.
20. High degeneracy of low-temperature states is indicated not only by the large value of the entropy plateau at $S_M \approx 1/3\, R\ln3$ at $T \sim 20$ K but also by the stiffness constant D. For ordinary antiferromagnets that order at $T \sim |\theta_W|$, the stiffness D_0 is estimated by the relation $D_0{}^2 \approx [3\sqrt{3}\zeta(3)/4\pi](ak_B\theta_W/\hbar)^2/\ln(2S + 1)$, with $\zeta(3) = 1.202$. In our case, the observed D was 850 m/s, nearly three times smaller than the expected D_0 of 2500 m/s, indicating softening due to magnetic frustration.
21. M. Imada, T. Mizusaki, S. Watanabe, available at http://arxiv.org/abs/cond-mat/0307022 (2003).
22. T. Kashima, M. Imada, *J. Phys. Soc. Jpn.* **70**, 3052 (2001).
23. H. Kawamura, S. Miyashita, *J. Phys. Soc. Jpn.* **53**, 4138 (1984).
24. P. Chandra, P. Coleman, *Phys. Rev. Lett.* **66**, 100 (1991).
25. G. H. Wannier, *Phys. Rev.* **79**, 357 (1950).
26. M. F. Collins, O. A. Petrenko, *Can. J. Phys.* **75**, 605 (1997).
27. K. Takeda, K. Miyake, K. Takeda, K. Hirakawa, *J. Phys. Soc. Jpn.* **61**, 2156 (1992).
28. J. A. Wilson, in *Metallic and Nonmetallic States of Matter*, P. P. Edwards, C. N. R. Rao, Eds. (Taylor and Francis, London, 1985), pp. 215–260.
29. J. A. Beattie, *J. Math. Phys.* **6**, 1 (1926/1927).
30. We thank J. Y. Chan, S. Fujimoto, K. Ishida, K. Kitagawa, R. T. Macaluso, D. E. MacLaughlin, R. Moessner, S. Sondhi, and O. Tchernyshyov for fruitful discussions. Work at Kyoto University supported in part by Grants-in-Aid for Scientific Research from the Japan Society for the Promotion of Science and for the 21st Century Center of Excellence "Center for Diversity and Universality in Physics" from the Ministry of Education, Culture, Sports, Science and Technology (MEXT) of Japan and by the Inamori Foundation. Work at Johns Hopkins University was supported by the U.S. Department of Energy.

Conversion of Zinc Oxide Nanobelts into Superlattice-Structured Nanohelices

Pu Xian Gao,[1] Yong Ding,[1] Wenjie Mai,[1] William L. Hughes,[1] Changshi Lao,[1] Zhong Lin Wang[1,2,3]*

A previously unknown rigid helical structure of zinc oxide consisting of a superlattice-structured nanobelt was formed spontaneously in a vapor-solid growth process. Starting from a single-crystal stiff nanoribbon dominated by the c-plane polar surfaces, an abrupt structural transformation into the superlattice-structured nanobelt led to the formation of a uniform nanohelix due to a rigid lattice rotation or twisting. The nanohelix was made of two types of alternating and periodically distributed long crystal stripes, which were oriented with their c axes perpendicular to each other. The nanohelix terminated by transforming into a single-crystal nanobelt dominated by nonpolar (01$\bar{1}$0) surfaces. The nanohelix could be manipulated, and its elastic properties were measured, which suggests possible uses in electromechanically coupled sensors, transducers, and resonators.

Helical structures have been observed for a number of inorganic materials. For example, carbon nanotube coils (1) are created when

paired pentagon-heptagon atomic rings arrange themselves periodically within the hexagonal carbon network (2). Formation of nanosprings

of amorphous silica has been thought to occur through a perturbation during the growth of a straight nanowire (*3*). Helical structures of SiC are proposed to be a screw-dislocation-driven growth process (*4*). By using the difference in surface stress on the two surfaces, rings and tubes of strained bilayer thin films, such as Si/SiGe, have been made (*5*).

Zinc oxide, an important semiconductive and piezoelectric material with several applications in optoelectronics and sensing, can form single-crystal nanosprings (*6*), nanorings (*7*), and nanobows (*8*) by bending or folding polar-surface-dominated nanobelts. These growth processes are dominated by a minimization of the electrostatic energy contributed by the cation- and anion-terminated surfaces of this ionic material, and their shapes are determined by balancing the electrostatic energy with the elastic deformation energy. The structural configurations of ZnO nanoobjects (*9*) could form the basis for fabricating nanoscale sensors, transducers, and resonators.

We now report a distinctive helical structure of ZnO made of a superlattice-structured nanobelt that is formed spontaneously in a solid-vapor growth process. The superlattice nanobelt is a periodic, coherent, epitaxial, and parallel growth of two alternating nanostripes of ZnO crystals oriented with their *c* axes perpendicular to each other. The role played by polar surfaces in the structural transformation is demonstrated, and the nanohelix has been manipulated by atomic force microscopy (AFM) to measure its elastic properties.

The ZnO nanohelices were grown with high reproducibility by a vapor-solid process (*10*) and by using temperature to control growth kinetics. The experimental setup consists of a horizontal high-temperature tube furnace, an alumina tube, a rotary pump system, and a gas-controlling system. First, 2 g of commercial ZnO powder (Alfa Aesar, Ward Hill, MA) were compacted, loaded into an alumina boat, and positioned at the center of the alumina tube as the source material. The system was prepumped to $\sim 2 \times 10^{-2}$ mbar, and the ramp rate was controlled at 20°C/min to 25°C/min when the temperature was raised from room temperature to 800°C. The furnace was then held at 800°C for 20 min, and the temperature was ramped at 20°C/min from 800° to 1400°C. When the temperature reached 1000°C, argon was introduced as a carrier gas to raise the pressure from $\sim 2 \times 10^{-2}$ mbar to the desired synthesis pressure of 200 to 250 mbar within $\sim$2.5 min. The solid-vapor deposition was carried out at 1400°C for ~ 2

[1]School of Materials Science and Engineering, Georgia Institute of Technology, Atlanta, GA 30332–0245, USA. [2]College of Engineering, Peking University, Beijing, China. [3]National Center for Nanoscience and Technology of China, Beijing 100080, China.

*To whom correspondence should be addressed. E-mail: zhong.wang@mse.gatech.edu

hours under a pressure of 200 to 250 mbar. The argon carrier gas was kept at a flow rate of 50 sccm (standard cubic centimeters per minute). The as-grown nanohelices of ZnO were deposited onto a polycrystalline Al_2O_3 substrate at a local temperature of 700° to 800°C and characterized by a variety of microscopes, including scanning electron microscopy (SEM) [LEO 1530 FEG (Oberkochen, Germany) at 5 and 10 kV], high-resolution transmission electron microscopy (TEM) [Hitachi HF-2000 at 200 kV and JEOL 4000EX (Tokyo, Japan) at 400 kV], AFM [Molecular Force Probe MFP-3D from Asylum Research (Santa Barbara, CA)], and focused ion beam microscopy (FIB) (FEI NOVA 200).

The as-synthesized sample was composed of up to 10% of freestanding nanohelices (fig. S1). High-resolution SEM images show the high degree of uniformity of the nanohelices, which can be left- (Fig. 1, A and C) or right-handed (Fig. 1, B and D). Their population ratio is nearly 1:1 (fig. S2). As shown in Fig. 1, the nanohelix diameters, widths, and pitch distances range between 300 to 700 nm, 100 to 500 nm, and 500 to 2500 nm, respectively (*11*). The length of the nanohelix can be as long as 100 μm. Energy dispersive x-ray spectroscopy analysis indicates that the nanorings are ZnO without detectable impurity.

Low-magnification TEM images of the nanohelices (Fig. 2, A and B) revealed the crystalline structure and winding shape of the nanobelts. The electron diffraction (ED) pattern, acquired from a single period of a nanohelix, shows mirror symmetry. This mirror symmetry is caused by superposition of several ZnO diffraction patterns rotated around the axial direction of the nanohelix axial direction of the nanohelix. A dark-field TEM image recorded from a segment of a nanobelt (Fig. 2C) shows that the nanobelt has a periodic superlattice structure across its entire width, with a uniform periodicity of ~3.5 nm. With a 5° offset, the stripes are nearly parallel to the nanobelt growth direction and run along the length of the nanohelix (fig. S3).

From crystallography, the wurtzite-structured ZnO crystal is described schematically as a number of alternating planes of tetrahedrally coordinated O^{2-} and Zn^{2+} ions stacked alternatively along the *c* axis. The oppositely charged ions produce positively charged (0001)-Zn^{2+} and negatively charged (000$\bar{1}$)-O^{2-} polar surfaces (*c* planes) (*7*, *9*). High-resolution TEM revealed the superlattice structure of the nanobelt with a periodic alternating arrangement of two types of stripes (Fig. 2D), which are oriented epitaxially in the following orientations: Stripe I has a growth direction of [1$\bar{1}$00], with top and bottom surfaces ±(0001) (polar surfaces); stripe II has a growth direction of [2$\bar{1}\bar{1}$2], with top and bottom surfaces ±(01$\bar{1}$0) (nonpolar surfaces). The corresponding ED pattern of the nanobelt

shows that the growth directions of the two types of stripes have a small rotation of $\alpha \approx 4°$ (Fig. 2E), indicating that the adjacent stripes rotate in the plane of the nanobelt for the same magnitude of the angle when forming the superlattice. The angles between the ED spots also slightly deviate from the expected result of a large crystal and suggest rigid lattice twist in some atomic planes. The two stripes are coherent by aligning (0$\bar{1}$10) of stripe I with (0002) of stripe II at a lattice mismatch of 2.9% and ($\bar{2}$110) of stripe I with ($\bar{2}$110) of stripe II without lattice mismatch, so the interface energy is likely to be low. Viewing from the projected direction of the incident electron beam, we aligned the two stripes by facing ($\bar{1}\bar{1}$20) of stripe I parallel to the ($\bar{2}$116) of stripe II and aligned the [0001] of stripe I with [01$\bar{1}$0] of stripe II. The true interface is inclined with respect to the direction of the electron beam, so that the contrast at the
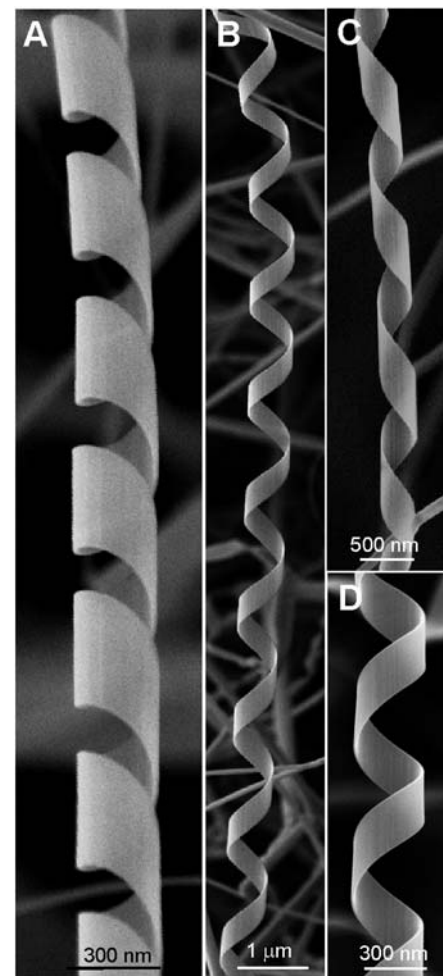
Fig. 1. Morphology of nanohelices. (**A** to **C**) Typical SEM images of the left- and right-handed ZnO nanohelices. (**D**) High-magnification SEM image of a right-handed ZnO nanohelix, showing a uniform and perfect shape. All of the nanohelices are directly received from the as-synthesized sample, and they are freestanding on the substrate surface.

interface in the high-resolution TEM image is not very sharp (Fig. 2F). On the basis of the orientation relation presented above, the experimental image can be simulated by using dynamic ED theory. The result is inserted in Fig. 2F (*11*), showing quantitative agreement with the observation. Thus, the interface for stripe I is likely to be ($\bar{1}\bar{1}22$) (*12*).

The initiation of the nanohelix is a direct result of superlattice formation. From an SEM image of a nanohelix with both ends (Fig. 3A), a straight stiff nanoribbon is directly connected to the starting point of a nanohelix. TEM examination shows that the joining point between the nanoribbon and the nanohelix is the place where the superlattice is created (Fig. 3B). The stiff nanoribbon is a single crystal object dominated by large *c*-plane surfaces (Fig. 3C). The superlattice is formed spontaneously and abruptly across the entire width of the nanoribbon. A striking feature is that the width of the nanobelt increases and its thickness decreases significantly after transforming into the superlattice structure (Fig. 3B and fig. S4). The stripes hold the same orientation relation as defined in Fig. 2E [see the selected-area ED (SAED) pattern inserted in Fig. 3C]. An enlarged local area shows the coexistence and spontaneous formation of two periodically arranged, alternating stripes at the transverse interface where the structural transformation occurred abruptly (Fig. 3D). At the transverse interface, the lattice mismatch of 2.9% between ($0\bar{1}10$) of the nanoribbon with (0002) of stripe II should create interface mismatch edge dislocations with a Burgers vector of [$0\bar{1}10$], which are expected to be separated by 3.45 nm. In fact, the periodicity of the superlattice is ~3.5 nm, and mismatch edge dislocations have been identified at the turning point between the nanoribbon and the superlattice (circled areas in Fig. 3D). The site of the mismatch dislocation could be the nucleation site of stripe II. The superior uniformity in periodicity of the superlattice is most likely to be a result of the lattice mismatch as defined by crystal structure, and rigid crystal twisting gives rise to the strain contrast observed in Fig. 3B and even in the high-resolution TEM image in Fig. 3D.

The termination of the nanohelix growth is caused by a complete conversion of the remaining polar surfaces into nonpolar surfaces and an increase in nanoribbon thickness. From the TEM image and the corresponding SAED patterns recorded from a single nanohelix (Fig. 3E), the formation of the nanohelix is a result of transforming a fully *c*-plane-dominated stiff nanoribbon (starting point) into a superlattice-structured, partially polar-surface-dominated flexible nanobelt (middle section). The starting stiff nanobelt is thick (~ 40 nm) and straight (fig. S4). After transforming into the superlattice-structured nanobelt, the thickness of the nanobelt is greatly reduced to less than


Fig. 2. Crystal structure of the nanohelix. (**A**) Typical low-magnification TEM image of a ZnO nanohelix, showing its structural uniformity. A straight nanobelt was enclosed inside the helix during the growth. (**B**) Low-magnification TEM image of a ZnO nanohelix with a larger pitch-to-diameter ratio. The selected-area ED pattern (SAEDP, inset) is from a full turn of the helix. (**C**) Dark-field TEM image from a segment of a nanohelix, showing that the nanobelt that coils into a helix is composed of uniformly parallel, longitudinal, and alternatively distributed stripes at a periodicity of ~3.5 nm across its entire width. The edge at the right-hand side is the edge of the nanobelt. (**D** and **E**) High-magnification TEM image and the corresponding SAEDP of a ZnO nanohelix with the incident beam perpendicular to the surface of the nanobelt, respectively, showing the lattice structure of the two alternating stripes. The SAEDP is composed of two sets of fundamental patterns, labeled and indexed in red for stripe I and yellow for stripe II. A careful examination of the image indicates that the true interface between the stripes is not edge-on in reference to the incident electron beam but at a relatively large angle. (**F**) Enlarged high-resolution TEM image showing the interface between the two adjacent stripes. The area within the dotted line is a simulated image using the dynamic electron diffraction theory. The interface proposed here is ($\bar{1}\bar{1}22$) for stripe I, which is inclined with respect to the incident electron beam at an angle of 32°.
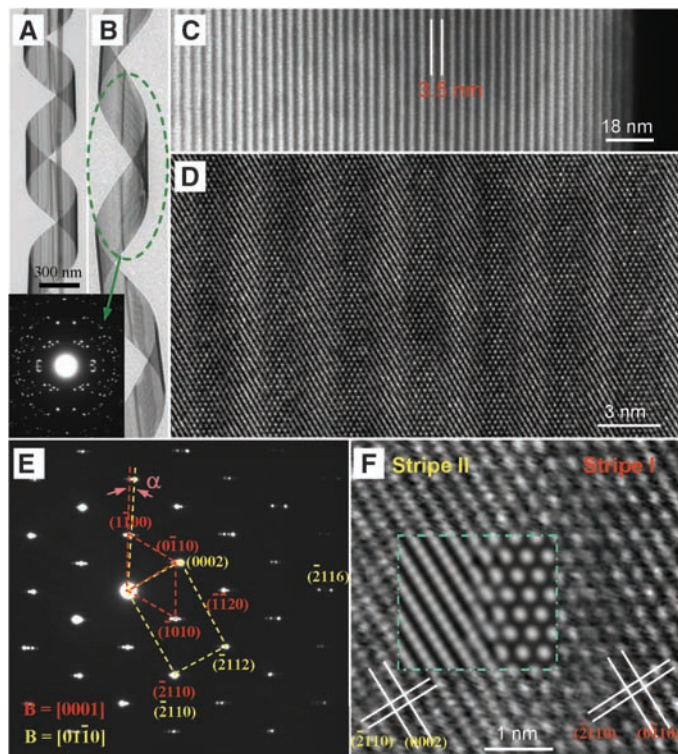
20 nm, and its width is substantially increased (fig. S4). Lastly, the ending of the nanohelix is a result of abruptly transforming the partially *c*-plane-dominated, superlattice-structured nanobelt into a single-crystal nanoribbon dominated by nonpolar surfaces at the finishing end (Fig. 3E), where the corresponding dark-field TEM image and the high-resolution TEM image (Fig. 3F) indicate that the top and bottom surfaces of the nanoribbon are the nonpolar ±($01\bar{1}0$) surfaces. The thickness of the nanoribbon increases significantly as well after transformation.

The formation of the nanohelix is a rigid structural alteration caused by the alternating stripes in the superlattice, and the formation of a superlattice is likely to be a polar charge–induced structural transformation (see the model in Fig. 3G). In the synthesis, a pre-pumping to 2×10^{-2} mbar creates the condition for growing polar surface–dominated nanoribbons (*13*). The polar charges are preserved on the surface during growth under conditions of high temperature and inert environment (*14*). As reported previously (*6*, *7*), the existence of the polar surfaces results in the formation of ZnO nanosprings and nanorings. If the width of the nanoribbon is rather large

(Fig. 3B), the electrostatic energy of the polar surfaces diverges with the extension of its length. A possible way of reducing the electrostatic energy is to transform the polar surface into a nonpolar surface, provided the interface mismatch energy is reasonably low, forming superlattice-structured stripes that are nearly parallel to the growth direction of the nanobelt. The introduction of argon gas at a later stage during the growth may be the initiation of superlattice formation. The switching in the *c* axis may indicate the formation of piezo-electric domains. The width of the nanobelt increases after the structural transformation from a single-crystal, *c*-plane-dominated stiff nanoribbon (in green) into a superlattice-structured, flexible nanobelt; the stripes are not exactly parallel to the growth direction of the nanobelt, and a small in-plane rotation for an angle of α exists between the growth directions of the two adjacent stripes, which induces the geometrical curvature required for rigidly twisting its shape. The polar charges remaining on the surfaces of stripe I also help to bend the nanobelt into a ring structure, especially with the decrease of the nanobelt thickness (*15*). Thus, the accumulation of rigid structural rotation or twist across the width of
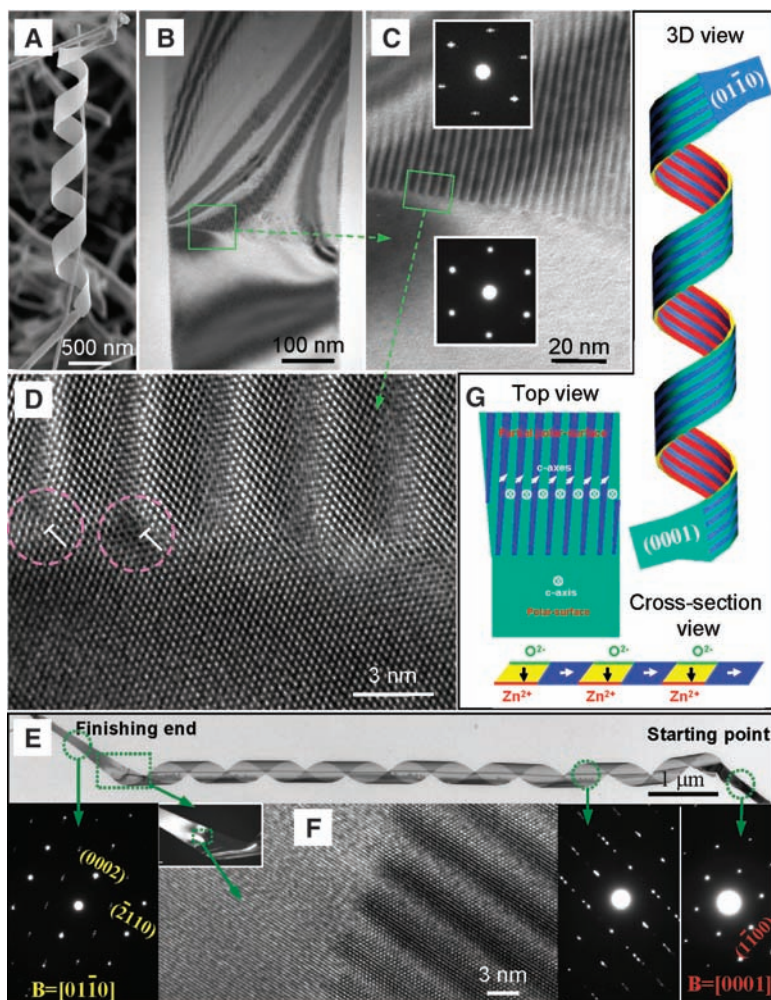
Fig. 3. Initiation and formation process of a nanohelix. (**A**) Low-magnification SEM image of a ZnO nanohelix showing its starting point and finishing end. (**B**) Low-magnification TEM image from the starting point of a nanohelix, showing a distinct and sharp contrast change across a transverse line and an increase in nanobelt width. (**C**) Enlargement of the boxed area in (B) and the corresponding diffraction patterns from the single crystal region (bottom inset) and the superlattice-structured region (top inset). The bottom segment is a *c* plane–dominated single-crystal stiff nanoribbon, whereas the top segment is a superlattice-structured flexible nanobelt, and the corresponding electron diffraction pattern is the same as the one shown in Fig. 2E. (**D**) High-magnification TEM image recorded from the interfacial region of the segments, showing a clear cutting line from where the structural transformation occurs across the entire width of the nanobelt. Mismatch edge dislocations are identified in the circled regions and directly linked to stripe II. (**E**) Low-magnification TEM image of a nanohelix showing its entire structure from beginning to end. Three representative SAEDPs are recorded from areas selected from the starting end, the middle section, and the finishing end. The starting point is a nanoribbon oriented along [0001], which is fully dominated by the *c*-plane polar surfaces; the middle section of the nanohelix is superlattice-structured, whereas the finishing end is a single-crystal nanoribbon that is dominated by nonpolar surfaces according to the dark-field TEM image (inset), [01$\bar{1}$0] diffraction pattern, and (**F**) high-resolution TEM image recorded from the area, where a distinct and clear-cut transformation from the superlattice-structured nanobelt to an *a*-plane-dominated nanoribbon is apparent. (**G**) Schematic models showing the top view and cross-sectional view of the nanobelt for illustrating the corresponding directions of the *c* axes and the distribution of polar charges (in green for O^{2-} and red for Zn^{2+}) and nonpolar surfaces (in blue). A three-dimensional (3D) structure model of a nanohelix, showing its initiating point and finishing end. The periodicity of the superlattices may result in the formation of periodic piezoelectric domains.

the superlattice nanobelt and a continuous growth of the stripes along the length of the nanobelt result in the formation of a helical structure, which could be left-handed or right-handed. The winding of the nanobelt is terminated after the nanobelt fully transforms from a partial-polar-surface-dominated and superlattice-structured nanoobject into a single-crystal nanoribbon dominated by nonpolar surface (in blue), which is likely to be caused by a change in growth kinetics. The single-crystal nanoribbon is a straight structure without rigid lattice alteration or surface polar charges; thus, it will not continue to wind but will extend as a straight ribbon.

Manipulation of a nanohelix with AFM and FIB shows that it has a rigid structure. A nanohelix has been sectioned by FIB into a short segment of one period (Fig. 4A), but the shape of the segment is still preserved and shows no visible relaxation. A nanohelix has also been cut by an AFM tip at two consecutive turns (Fig. 4C), and the preservation of the rigid shape by a single-turn helix after cutting suggests little, if any, stored elastic energy (*16*).

The transverse spring constant of the nanohelix, a quantity for describing the stiffness of

Fig. 4. Manipulation of a nanohelix and measurement of its elastic properties. (**A**) SEM image of a nanohelix that was cut by a FIB microscope shows the preservation of the rigid geometrical shape after the cut, which suggests there is minimal stored elastic energy. (**B**) AFM contact mode measurement of the sensitivity (*S*) of the photodetector for the silicon substrate and the four turns of a ZnO nanohelix, as indicated by 1 to 4 in the inserted AFM image. The sensitivity *S* of the photodetector is the inverse of the slope of the force-displacement (*F-Z*) curve, which is directly related to the elastic property. The measurement was done by positioning the tip on the surface of the upmost middle point of the turn of the helix. Each dot represents one measurement. The sensitivity S_{Si} for silicon is substantially lower than that for the ZnO nanohelix (S_{Helix}). (**C**) Fracture of the nanohelix at two consecutive turns of the nanohelix by the AFM tip, showing a preservation of helical shape in the sectioned region.
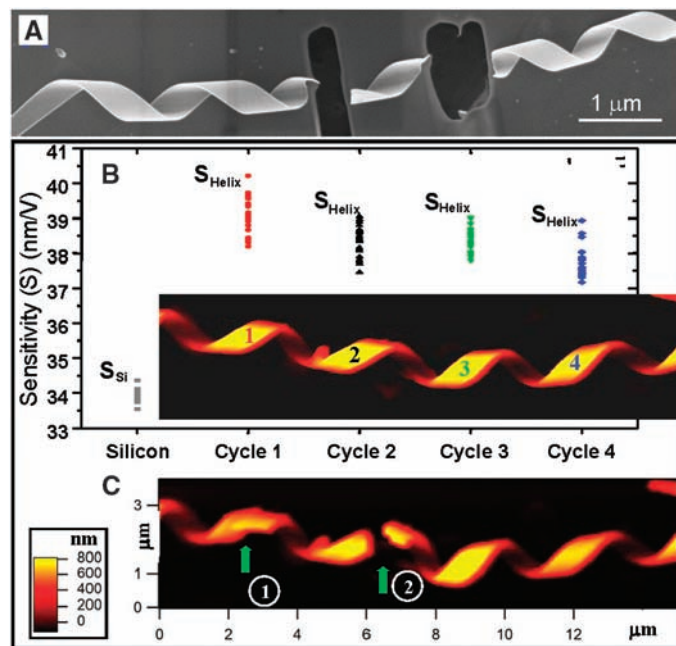
the nanohelix perpendicular to its axial direction, has been measured by AFM with use of the force-displacement (*F-Z*) curve (*17*). Through the static compression of a nanohelix lying on a silicon substrate with an AFM tip (Fig. 4B) (fig. S5) and careful calibration of the sensitivity, *S*, of the photodetector (*11*, *18*), which is the inverse of the slope of the *F-Z* curve (fig. S6), the transverse spring constant of the nanohelix, K_{Helix}, was found to be (*11*) 3.9, 4.6, 4.5, and 5.3 N/m for one to four turns, respectively, of the nanohelix as labeled in Fig. 4B. The measured K_{Helix} is near the theoretically estimated transverse spring constant of 4.2 N/m (*11*), and so the elastic modulus, E, values of the nanohelix derived from the measured spring constant (*11*) are 42, 49, 48, and 57 GPa for the four turns, respectively, which agrees well with the elastic modulus measured for straight ZnO nanobelts by mechanical resonance with the use of in situ TEM (*19*).

The perfect helix we observed is of great interest not only for understanding the growth behavior of polar-surface–driven growth processes in the wurtzite system, such as GaN, AlN, and InN, but also for investigating fundamental physics and optical phenomena. The piezoelectric and semiconducting properties of ZnO suggest that the nanohelix could be a fundamental unit for investigating electromechanically coupled nanodevices by using the

superlattice piezoelectric domains. The nanohelix is likely to have important applications in sensors, transducers, resonators, and photonics.

References and Notes

1. S. Amelinckx *et al.*, *Science* **265**, 635 (1994).
2. R. P. Gao, Z. L. Wang, S. S. Fan, *J. Phys. Chem. B* **104**, 1227 (2000).
3. H. F. Zhang, C. M. Wang, E. C. Buck, L. S. Wang, *Nano Lett.* **3**, 577 (2003).
4. H. F. Zhang, C. M. Wang, L. S. Wang, *Nano Lett.* **2**, 941 (2002).
5. O. G. Schmidt, K. Eberl, *Nature* **410**, 168 (2001).
6. X. Y. Kong, Z. L. Wang, *Nano Lett.* **3**, 1625 (2003).
7. X. Y. Kong, Y. Ding, R. Yang, Z. L. Wang, *Science* **303**, 1348 (2004).
8. W. L. Hughes, Z. L. Wang, *J. Am. Chem. Soc.* **126**, 6703 (2004).
9. Z. L. Wang *et al.*, *Adv. Funct. Mater.* **14**, 944 (2004).
10. Z. W. Pan, Z. R. Dai, Z. L. Wang, *Science* **291**, 1947 (2001).
11. See Materials and Methods provided on *Science* Online.
12. The {1̄122} are typical twin planes for ZnO (*20*).
13. P. X. Gao, Z. L. Wang, *Small*, in press; published online (http://dx.doi.org/10.1002/smll.200500165).
14. The growth of the nanostructure occurred at a local temperature of ~700° to 800°C in an argon atmosphere, under which the possibility of neutralizing the surface polar charges by adsorbing foreign molecules is unlikely, provided the growth occurred fairly quickly. This result is consistent with our previous studies [see (*7–9*)].
15. From the energy point of view, a polar-surface-dominated nanobelt tends to fold itself into a ring or spring for reducing electrostatic energy (*6*). The nanoring is stable if the ratio between nanobelt thickness, *t*, and the radius, *R*, of the nanoring is smaller than ~3% (*8*). Nanorings with *t/R* > 3% are energetically unfavorable to form.
16. The aforementioned data rule out the possibility that the nanohelix is formed by bilayer surface strain (*5*) for two reasons. First, there is no bilayer strained structure in our system; and second, the difference in surface stress on the (0001)-Zn and (0001̄)-O of ZnO, if any, has negligible effect on the formation of nanorings or nanobows (*8*). The nanohelix is likely to be formed by two processes: the rigid structural alteration due to the formation of the superlattice and the spontaneous polar-charge-induced bending (*6*). However, *t* of the nanobelt is ~20 nm, and typical *R* of the nanohelix is ~150 to 350 nm (Fig. 1). Thus the *t/R* is ~6 to 13%, which is much larger than the threshold value (~3%) permitted for forming a nanoring by electrostatic polar charges (*15*). Also, considering the great reduction in area of the polar surfaces (for ~50%) after forming the superlattice as well as the helical shape of the structure, the role played by polar charges in forming a helix is dramatically reduced. Therefore, the dominant mechanism for forming the nanohelix is by rigid lattice rotation and twisting as a result of superlattice formation.
17. E. W. Wong, P. E. Sheehan, C. M. Lieber, *Science* **277**, 1971 (1997).
18. A. Volodin *et al.*, *Phys. Rev. Lett.* **84**, 3342 (2000).
19. X. D. Bai, P. X. Gao, Z. L. Wang, E. G. Wang, *Appl. Phys. Lett.* **82**, 4806 (2003).
20. Y. Dai, Y. Zhang, Z. L. Wang, *Solid State Commun.* **126**, 629 (2003).
21. Thanks to support from NSF, the NASA Vehicle Systems Program and Department of Defense Research and Engineering, the Defense Advanced Research Projects Agency, and the Chinese Academy of Sciences.

Simulated Quantum Computation of Molecular Energies

Alán Aspuru-Guzik,[1]*† **Anthony D. Dutoi,**[1]* **Peter J. Love,**[2] **Martin Head-Gordon**[1,3]

The calculation time for the energy of atoms and molecules scales exponentially with system size on a classical computer but polynomially using quantum algorithms. We demonstrate that such algorithms can be applied to problems of chemical interest using modest numbers of quantum bits. Calculations of the water and lithium hydride molecular ground-state energies have been carried out on a quantum computer simulator using a recursive phase-estimation algorithm. The recursive algorithm reduces the number of quantum bits required for the readout register from about 20 to 4. Mappings of the molecular wave function to the quantum bits are described. An adiabatic method for the preparation of a good approximate ground-state wave function is described and demonstrated for a stretched hydrogen molecule. The number of quantum bits required scales linearly with the number of basis functions, and the number of gates required grows polynomially with the number of quantum bits.

Feynman observed that simulation of quantum systems might be easier on computers using quantum bits (qubits) (*1*). The subsequent development of quantum algorithms has made this observation concrete (*2–6*). On classical computers, resource requirements for complete simulation of the time-independent Schrödinger equation scale exponentially with the number of atoms in a molecule, limiting

such full configuration interaction (FCI) calculations to diatomic and triatomic molecules (*7*). Computational quantum chemistry is therefore based on approximate methods that often succeed in predicting chemical properties for larger systems, but their level of accuracy varies with the nature of the species, making more complete methods desirable (*8*).

Could quantum computation offer a new way forward for exact methods? Despite the formal promise, it has not been demonstrated that quantum algorithms can compute quantities of chemical importance for real molecular systems to the requisite accuracy. We address this issue by classically simulating quantum computations of the FCI ground-state energies of two small molecules. Although the basis sets used are small, the energies are obtained to the precision necessary for chemistry. Absolute molecular energies must be computed to a precision (greater than six decimal places) that reflects the smaller energy differences observed in chemical reactions (~0.1 kcal/mol). These simulations show that quantum computers of tens to hundreds of qubits can match and exceed the capabilities of classical FCI calculations.

A molecular ground-state energy is the lowest eigenvalue of a time-independent Schrödinger equation. The phase-estimation algorithm (PEA) of Abrams and Lloyd (*3*, *4*) can

[1]Department of Chemistry, University of California, Berkeley, CA, USA. [2]D-Wave Systems, Inc., 4401 Still Creek Drive, Suite 100, Burnaby, BC V5C 6G9, Canada. [3]Chemical Sciences Division, Lawrence Berkeley National Laboratory, Berkeley, CA 94720, USA.

*These authors contributed equally to this work.
†To whom correspondence should be addressed. E-mail: alan@aspuru.com